Int J Thermophys (2010) 31:2380–2393
DOI 10.1007/s10765-010-0808-7

Comparison of Thermal Conductivity and Thermal Boundary Conductance Sensitivities in Continuous-Wave and Ultrashort-Pulsed Thermoreflectance Analyses

Patrick E. Hopkins · Justin R. Serrano · Leslie M. Phinney

Received: 25 June 2009 / Accepted: 28 July 2010 / Published online: 12 August 2010

Abstract Thermoreflectance techniques are powerful tools for measuring thermophysical properties of thin film systems, such as thermal conductivity, Λ, of individual layers, or thermal boundary conductance across thin film interfaces (G). Thermoreflectance pump–probe experiments monitor the thermoreflectance change on the surface of a sample, which is related to the thermal properties in the sample of interest. Thermoreflectance setups have been designed with both continuous wave (cw) and pulsed laser systems. In cw systems, the phase of the heating event is monitored, and its response to the heating modulation frequency is related to the thermophysical properties; this technique is commonly termed a phase sensitive thermoreflectance (PSTR) technique. In pulsed laser systems, pump and probe pulses are temporally delayed relative to each other, and the decay in the thermoreflectance signal in response to the heating event is related to the thermophysical properties; this technique is commonly termed a transient thermoreflectance (TTR) technique. In this work, mathematical models are presented to be used with PSTR and TTR techniques to determine the Λ and G of thin films on substrate structures. The sensitivities of the models to various thermal and sample parameters are discussed, and the advantages and disadvantages of each technique are elucidated from the results of the model analyses.

Keywords Continuous wave laser · Phase sensitive thermoreflectance · Thermal boundary conductance · Thermal conductivity · Thermoreflectance · Thin films · Transient thermoreflectance · Ultrashort pulsed laser

P. E. Hopkins (✉) · J. R. Serrano · L. M. Phinney
Engineering Science Center, Sandia National Laboratories, Albuquerque, NM 87185-0346, USA
e-mail: pehopki@sandia.gov

1 Introduction

As nanomaterials and systems continue to decrease in characteristic dimensions, a fundamental understanding of the thermal processes driving transport is becoming ever-more critical for continued progress in device design and engineering [1]. However, decreasing length scales increase experimental challenges in thermal measurements [2,3]. For example, traditional electrical contact-based experimental techniques for measuring thermal transport, such as steady-state Joule heating [4,5] or the 3ω method [6,7], are subject to contact resistances that can greatly complicate analyses of thermal transport in nanostructures [8–10]. Therefore, optical-based measurement techniques have an advantage over electrical contact-based techniques due to their non-contact nature. However, thermal analyses and signal interpretation of optical-based techniques are much more complicated than electrical contact-based techniques [11].

In this paper, we derive and compare models for two different optically based experimental techniques used to measure the thermal boundary conductance, G, and thermal conductivity, Λ, in nanofilm systems: phase sensitive thermoreflectance (PSTR) and transient thermoreflectance (TTR). Both the PSTR and TTR techniques utilize a pump–probe experimental geometry. Where the PSTR technique uses continuous wave (cw) lasers and monitors the change in the probe phase as a function of frequency, the TTR technique involves short pulsed laser systems and tracks the change in the probe signal as a function of time by changing the pump or probe path length. Both the PSTR [12–16] and TTR techniques [17–22] have been extensively used by several research groups to measure thermal transport in nanosystems. To directly compare the advantages and disadvantages between the PSTR and TTR techniques, we derive models using similar assumptions for each technique and fundamental heat transport theory in the next section. In Sect.3, we parametrically study the sensitivities of the models to thermal boundary conductance and thermal conductivity.

2 Thermal and Signal Analyses

Both the PSTR and TTR techniques use a modulated pump laser as a heating source and monitor the change in temperature on the surface of the structure resulting from the modulated source. To determine the temperature rise, and due to the cylindrical symmetries of the lasers, we start with the heat equation in cylindrical coordinates, given by

$$C\frac{\partial\theta\left(z,t\right)}{\partial t}=\Lambda_z\frac{\partial^2\theta\left(z,t\right)}{\partial z^2}+\frac{\Lambda_r}{r}\frac{\partial}{\partial r}\left(r\frac{\partial\theta\left(z,t\right)}{\partial r}\right), \tag{1}$$

where C is the heat capacity, θ is the temperature rise, t is the time, r is the radial coordinate, and the subscripts r and z denote the radial and cross-plane conductivities. Taking the Hankel transform, then the Fourier transform of Eq. 1 leads to

$$\frac{\partial^2\theta(\omega)}{\partial z^2} = q^2\theta(\omega), \tag{2}$$

where ω is the angular frequency of the heating event and

$$q^2 = \frac{\Lambda_r k^2 + \mathrm{i}C\omega}{\Lambda_z}, \tag{3}$$

where k is the transform variable. This anisotropic q can be used to determine the directionally dependent thermal conductivities in anisotropic structures [23]. In isotropic structures,

$$q^2 = k^2 + \frac{\mathrm{i}C\omega}{\Lambda_z}. \tag{4}$$

Given Eq. 3 or 4, the temperature at the surface of a material is easily taken into account through Carslaw and Jaeger's solution for a steady periodic temperature change in composite slabs [24]. A convenient implementation of this is presented by Feldman [25] and discussed here. The change in the surface temperature in a material is given by

$$F(k) = \frac{1}{\gamma_1}\left(\frac{F_{T1}^{+} + F_{T1}^{-}}{F_{T1}^{-} - F_{T1}^{+}}\right), \tag{5}$$

where F_{T1}^{+} and F_{T1}^{-} are temperature change coefficients related to the forward and backward propagating waves on the surface (top side) of material 1 and $\gamma = \Lambda q$ with $F(k)$ being the change in surface temperature. Here, we take the topmost material (or the material being directly probed) as material 1 as we will consider multilayer configurations in the following subsections. The forward and backward propagating waves at the top side of material 1 are related to the waves on the bottom side through

$$\begin{bmatrix} F_{T1}^{+} \\ F_{T1}^{-} \end{bmatrix} = \begin{bmatrix} \exp[-q_1 d_1] & 0 \\ 0 & \exp[q_1 d_1] \end{bmatrix} \begin{bmatrix} F_{B1}^{+} \\ F_{B1}^{-} \end{bmatrix}, \tag{6}$$

where d is the material thickness. Boundary conditions at the bottom side of the material are required to determine the change in the surface temperature, which are addressed in the next subsections.

To determine the three-dimensional (3D) temperature oscillations on the surface of material 1 due to cooling from underlying materials described by Eq. 5, a top surface boundary condition must be imposed. In pump–probe laser experiments, this is described by first convoluting Eq. 5 with the pump-beam distribution [23], given by

$$\theta(k) = F(k)\frac{A}{2\pi}\exp\left[\frac{-k^2 w_{\mathrm{m}}^2}{8}\right], \tag{7}$$

where A is the absorbed power from the pump beam and w_{m} is the $1/\mathrm{e}^2$ radius of the pump beam, and then taking the weighted average of the surface temperature oscillations by the probe beam of $1/\mathrm{e}^2$ radius w_{r} [26] to yield

$$\theta(\omega) = \frac{A}{2\pi} \int_0^\infty F(k) \exp\left[\frac{-k^2\left(w_{\mathrm{m}}^2 + w_{\mathrm{r}}^2\right)}{8}\right] k\mathrm{d}k. \tag{8}$$

Equation 8 gives the change in temperature as a function of the heating event modulation frequency at the surface of the film.

2.1 Temperature Change During TTR

Short pulsed transient TTR experiments typically utilize high repetition rate laser systems with pump modulation frequencies, f, ranging from 0.1 MHz to 10 MHz. Since the change in temperature in TTR experiments is determined over the pump–probe delay time, which in TTR experiments is typically no more than 8 ns due to experimental error introduced by the physical path delay, the boundary condition of the back side of the material is related to the lifetime of the temperature decay. The spatial extent of the temperature gradient is determined by the thermal penetration depth, given by $D = \sqrt{\Lambda/(C\pi f)}$, where f is the modulation frequency of the heating event (pump). The thermal diffusion time, which is related to the Fourier number, represents the time it takes for heat to diffuse over the given distance, L, is given by $\tau = L^2 C/\Lambda$ [27]. Therefore, the time it takes for heat to diffuse over the thermal penetration depth is given by $\tau = 1/(\pi f)$. As long as $\tau <$ the pump–probe delay time (which is typically 8 ns as previously mentioned), then the substrate can be assumed semi-infinite; this criterion is upheld for the typical pump modulation frequencies in TTR. Assuming a semi-infinite material, heat cannot reach the bottom side of slab 2, so there is no thermal buildup of waves and

$$\begin{bmatrix} F_{T1}^{+} \\ F_{T1}^{-} \end{bmatrix} = \begin{bmatrix} 0 \\ \exp\left[-u_2 d_2\right] \end{bmatrix} \tag{9}$$

which is used to determine the frequency response to the temperature rise *via* Eqs. 5 and 8.

For a thin film on a bulk substrate, the analytical solution to the thermal diffusion equation must take into account transport in two adjacent media. For material 1, the top side is assumed at the slab/air interface and the bottom side is assumed as the interface between material 1 and material 2 (i.e., film/substrate). Given a thermal boundary conductance, G, between material 1 and material 2, the temperature at the top of slab 2 is related to the temperature at the bottom side of slab 1 by

$$\begin{bmatrix} F_{B1}^{+} \\ F_{B1}^{-} \end{bmatrix} = \frac{1}{2} \begin{bmatrix} 1 + \frac{\gamma_2}{\gamma_1} - \frac{\gamma_2}{G_{12}} & 1 - \frac{\gamma_2}{\gamma_1} + \frac{\gamma_2}{G_{12}} \\ 1 - \frac{\gamma_2}{\gamma_1} - \frac{\gamma_2}{G_{12}} & 1 + \frac{\gamma_2}{\gamma_1} + \frac{\gamma_2}{G_{12}} \end{bmatrix} \begin{bmatrix} F_{T2}^{+} \\ F_{T2}^{-} \end{bmatrix}. \tag{10}$$

Assuming a bulk substrate, heat cannot reach the bottom side of slab 2 at rates comparable to the modulation frequency (as previously mentioned), so

$$\begin{bmatrix} F_{T2}^{+} \\ F_{T2}^{-} \end{bmatrix} = \begin{bmatrix} 0 \\ \exp\left[-u_2 d_2\right] \end{bmatrix}. \tag{11}$$

Figure 1 shows the change in temperature as a function of frequency for bulk Al, a 100 nm Al film on a bulk Si substrate, and a 100 nm Al film on a bulk SiO_2 substrate. The thermal properties of the materials of interest are listed in Table 1. For all calculations in this work, pump and probe spot sizes of 25 μm and an absorbed pump power of 1 mW are assumed. The real component of the temperature rise, shown by the solid line, is associated with the steady-state temperature rise, and the imaginary component of the temperature rise, shown by the dashed line, is associated with the periodic temperature rise from the modulated source. Note that the imaginary

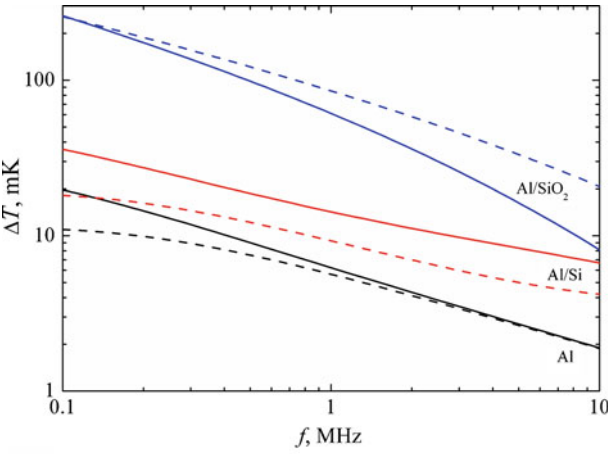

Fig. 1 Change in temperature on the surface of bulk Al, 100 nm Al film on a Si substrate, and 100 nm Al film on a SiO_2 substrate as a function of pump modulation frequency. The real component (*solid line*) is associated with the steady-state temperature rise, while the imaginary component (*dashed line*) is related to the periodic temperature rise due to the thermal oscillations. Note that the imaginary component of the temperature rise shown in this figure represents the absolute value since the imaginary component of the temperature rise is negative. These calculations simulate the TTR response so the substrate is assumed semi-infinite

Table 1 Thermophysical properties of Al, Si, and SiO_2 at 300 K [31]

	Λ ($W \cdot m^{-1} \cdot K^{-1}$)	C ($MJ \cdot m^{-3} \cdot K^{-1}$)
Al	237	2.44
Si	148	1.66
SiO_2	1.38	1.65

Thermal boundary conductances, G, at the Al/Si and Al/SiO_2 interfaces are 100 $MW \cdot m^{-2} \cdot K^{-1}$ [30] and 50 $MW \cdot m^{-2} \cdot K^{-1}$ [29], respectively

component of the temperature rise shown in Fig. 1 represents the absolute value since the imaginary component of the temperature rise is negative.

The output of the lock-in amplifier serves to relate frequency domain models to the time domain. The lock-in output will be the magnitude, R, and phase, φ, of the probe signal at the heating event modulation frequency. Because the width of the optical pulses produced by a oscillator laser cavity typically used in TTR (on the order of 100 fs) is much shorter than the time scales of interest when determining the thermal conductivity and thermal boundary conductance (100 ps to a few nanoseconds), we can approximate the frequency spectrum of the laser output as a series of delta functions separated in frequency by the repetition rate of the laser which leads to the mathematical form of the lock-in output of [23]

$$R \exp\left[\mathrm{i}\left(\omega_{\mathrm{m}} t + \phi\right)\right] = Z\left(\omega_{\mathrm{m}}\right) \exp\left[\mathrm{i}\omega_{\mathrm{m}} t\right], \tag{12}$$

where ω_{m} is the angular modulation frequency of the pump pulses, t is the time, ϕ is the phase, and $Z(\omega_0)$ is the transfer function of the lock-in. In the frequency domain, the transfer function can be represented as [26]

$$Z\left(\omega_0\right) = \frac{(2\pi)^2 \chi}{\omega_{\mathrm{s}}^2} \sum_{M=-\infty}^{\infty} \theta\left(\omega_0 + M\omega_{\mathrm{s}}\right) \exp\left[\mathrm{i}M\omega_{\mathrm{s}}\tau\right], \tag{13}$$

where ω_{s} is the modulation frequency of the laser system (not the modulation frequency of the heating event, so for a Ti:Sapphire oscillator, $\omega_{\mathrm{s}}/2\pi$ is approximately 80 MHz), τ is the delay time between the pump and probe pulses, and χ is a constant that is related to the gain of the electronics, the power of the pump and probe pulses, and the thermoreflectance coefficient of the material. From Eq. 13, the lock-in outputs are given by

$$X = \mathrm{Re}\left[Z\left(\omega_0\right)\right], \quad Y = \mathrm{Im}\left[Z\left(\omega_0\right)\right], \tag{14}$$

where X and Y are the real and imaginary components of the measured frequency response.

Figure 2 shows the measured lock-in signal $(-X/Y)$ as a function of the pump probe delay time for a modulation frequency of 1 MHz. We choose the TTR analysis at $f = 1$ MHz since it represents the middle of the modulation frequency range typically used in experiments. A detailed analysis of the effects of the modulation frequency on the measured TTR signal is discussed by Schmidt et al. [23]. Figure 2 shows the TTR signal as a function of time, which is related to the temperature change *via* Eq. 13, as a function of the pump–probe delay time for the three material systems shown in Fig. 1.

2.2 Temperature Change During PSTR

In PSTR experiments, the probe reflectance as a function of the pump modulation frequency is monitored by the lock-in amplifier. The change in the lock-in signal from

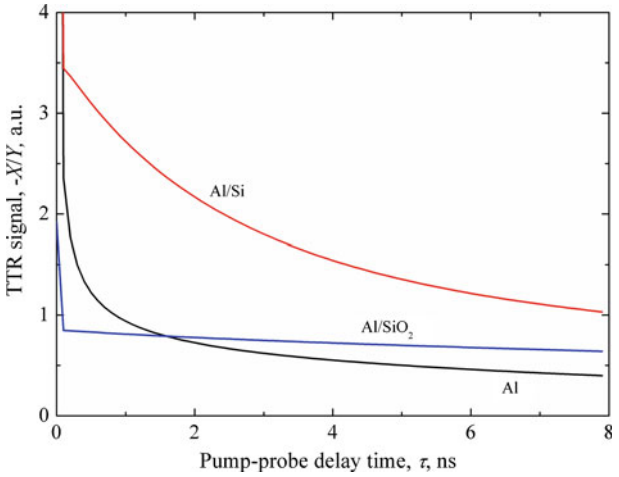

Fig. 2 Simulated TTR signal from the lock-in as a function of pump–probe delay time

that of the probe is typically related to a thermal model to determine thermophysical properties. The lock-in signal is indicative of the change in the probe due to the thermal wave traveling in the material of interest. Typically in PSTR, the heating event is modulated at relatively low frequencies compared to TTR experiments since the PSTR signal is larger at lower frequencies due to larger temperature changes (1 Hz to 10 kHz). Although PSTR can be used at high frequencies, similar to those in TTR, due to the relatively low signal at these high frequencies, signal-to-noise ratios are quite small leading to uncertainties in thermophysical-property determinations.

As with the TTR analysis, we must specify a back-side boundary condition for the PSTR analysis. Typical material systems of interest have film on substrate geometries, with thicknesses dominated by the substrate, typically on the order of 500 μm. For a highly conductive substrate, such as Si, D will range from 5 000 μm to 50 μm over the 1 Hz to 10 kHz modulation range. For an insulative substrate, such as SiO_2, D will range from 500 μm to 5 μm. Since the penetration depth is greater than or on the same order as typical substrate thicknesses, PSTR analyses cannot assume a semi-infinite substrate and the back-side boundary condition must be specified. Here, we assume that the back side of the material of interest is insulated, which is a valid assumption when the material is probed with air as the surrounding medium.

To account for an insulative boundary in the algorithm discussed in Sect. 2.1, we assume an infinite thermal boundary conductance between material 2 (the material furthest away from the pump-probe surface) and material 3 (medium) and that material 3 has the same thermophysical properties as material 2. Therefore, Eq. 10 becomes

$$\begin{bmatrix} F_{B2}^{+} \\ F_{B2}^{-} \end{bmatrix} = \begin{bmatrix} 1 & 0 \\ 0 & 1 \end{bmatrix} \begin{bmatrix} F_{T3}^{+} \\ F_{T3}^{-} \end{bmatrix}. \tag{15}$$

To model a completely insulative back-side, the temperature gradient must be forced to zero in material 3 (the medium, or air), so the temperature coefficients on the "top side" of material 3 are given by

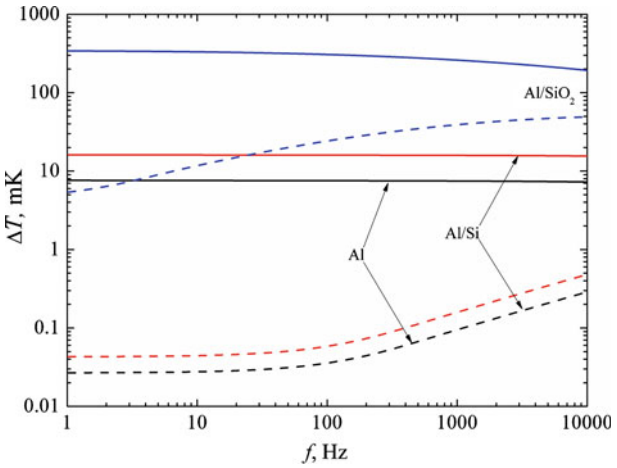

Fig. 3 Change in temperature as a function of pump modulation frequency for a 500 μm Al film, a 100 nm Al film on a 500 μm Si substrate, and a 100 nm Al film on a 500 μm SiO_2 substrate. These calculations simulate the PSTR response, so the back boundary of the substrate is assumed insulative. The real component (*solid line*) is associated with the steady-state temperature rise while the imaginary component (*dashed line*) is related to the periodic temperature rise due to the thermal oscillations

$$\begin{bmatrix} F_{T2}^{+} \\ F_{T2}^{-} \end{bmatrix} = \begin{bmatrix} 1 \\ 1 \end{bmatrix}, \tag{16}$$

which is the insulative version of Eq. 11.

Figure 3 shows the change in temperature as a function of frequency for a 500 μm Al film, a 100 nm Al film on a 500 μm Si substrate, and a 100 nm Al film on a 500 μm SiO_2 substrate. Since the PSTR technique analyzed in this model utilizes cw laser systems (unmodulated), the lock-in output does not represent the summation over higher harmonics, and $Z(\omega_0) = \chi\theta(\omega_0)$. Typically, PSTR analyses analyze the phase of the lock-in output. Here, we examine the ratio discussed in Fig. 2, as this is essentially the same as examining the phase ($\phi = \tan^{-1}[-Y/X]$). Figure 4 shows the PSTR signal as a function of frequency. The Al and Al/Si systems are similar since both are very thermally conductive. The PSTR signal on the Al/SiO_2 system differs from the other systems due to the thermally insulative properties of SiO_2 and the small thermal boundary conductance.

3 Model Sensitivities

The sensitivities of the TTR and PSTR techniques to a given model parameter, ξ, are described by [28]

$$S_\xi = \frac{\partial \ln\left[\frac{-X}{Y}\right]}{\partial \ln[\xi]} = \frac{\xi}{\left(\frac{-X}{Y}\right)} \frac{\partial\left[\frac{-X}{Y}\right]}{\partial[\xi]}. \tag{17}$$

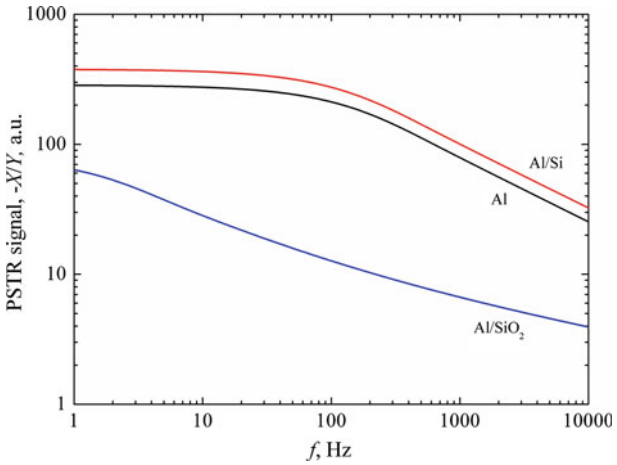

Fig. 4 Simulated PSTR signal from the lock-in as a function of pump modulation frequency for the material systems studied in Fig. 3

In this work, we are interested in the sensitivities of the two techniques to the thermal conductivity and film/substrate thermal boundary conductance, so $\xi = \Lambda$ or G. Sensitivities of PSTR and TTR to Λ and G are shown in Fig. 5. For this work, we assume a TTR modulation frequency of 1 MHz; however, this frequency can be adjusted which can change the sensitivity [23]. PSTR is sensitive to the thermal conductivity of Si at high frequencies and that of SiO_2 at low frequencies. As the thermal conductivity of the substrate decreases, the peak sensitivity shifts to lower frequencies. The TTR technique is sensitive to the thermal conductivities over all delay times. PSTR is not sensitive to G at the Al/SiO_2 interface at any frequencies, and the sensitivity to G at the Al/Si interface is independent of frequency. This is the same result found in studies utilizing the 3ω method [8,29]. The TTR technique is slightly sensitive to G at the Al/SiO_2 interface and shows dynamic sensitivity over the delay time to G at the Al/Si interface. Note that, for this sensitivity analysis, the positive or negative value of the sensitivity is meaningless, only the absolute value determines how "sensitive" the thermal transport is to a given parameter in each technique.

Although Si and SiO_2 are two thermally different material systems that give different responses in both the PSTR and TTR techniques, a parametric study of the sensitivities of PSTR and TTR to G and Λ will provide insight into the underlying thermophysics driving the measurements. Figure 6 shows the measurement sensitivity calculations from Fig. 5 for a range of different substrate thermal diffusivities (Λ/C) and thermal boundary conductances of a 100 nm Al film on substrate system. The thermal diffusivities roughly correspond to a range of thermal conductivities representing water on the low end and diamond on the high end. When calculating S_Λ, it is assumed that $G = 100\ \mathrm{MW \cdot m^{-2} \cdot K^{-1}}$ and $C = 1\ \mathrm{MJ \cdot m^{-3} \cdot K^{-1}}$; when calculating S_G, Λ is assumed as $100\ \mathrm{W \cdot m^{-1} \cdot K^{-1}}$ and C is assumed as $1\ \mathrm{MJ \cdot m^{-3} \cdot K^{-1}}$ (i.e., the thermal diffusivity is assumed as $1 \times 10^{-4}\ \mathrm{m^2 \cdot s^{-1}}$). This value of G is assumed when calculating S_Λ since it represents an average value commonly observed between nanofilms [1,30], and this value of Λ is assumed when calculating S_G since it roughly

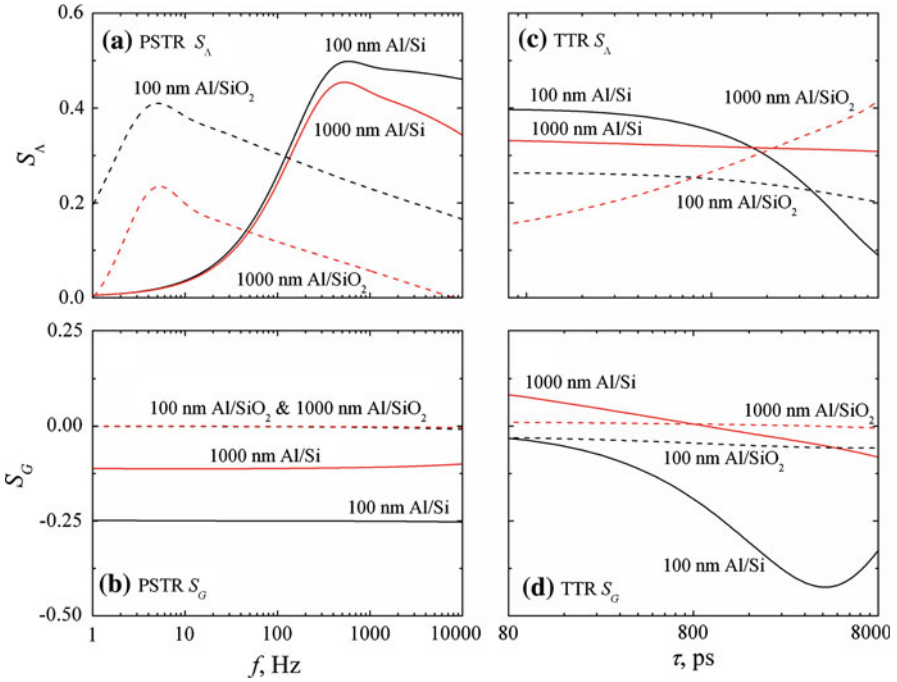

Fig. 5 Sensitivities of the PSTR and TTR responses using Eq. 17. Note that the PSTR sensitivities are graphed in the frequency domain and the TTR sensitivities are graphed in the time domain. Both models show sensitivity to the various thermophysical properties of interest in the material systems simulated here. G is inherently insensitive in the frequency domain (PSTR) for Al/Si and Al/SiO_2, which follows previous results [8,29]

corresponds to the thermal conductivity of Si, which is the most common material used in nanodevices. Over the frequency domain of interest in PSTR and the time domain of interest in TTR, the thermal properties of the Al film do not drastically affect the sensitivity calculations in this work. For example, in PSTR, the typical modulation frequencies used in experiments range from 1 Hz to 10 kHz. This corresponds to a thermal penetration depth, D, in the sample with the lowest diffusivity of 5.64 μm at 10 kHz. This penetration depth is bigger for the larger diffusivity samples and lower modulation frequencies. Therefore, the 100 nm Al film only represents a small fraction of the overall "sampled" region in the material and will not affect the calculations. In TTR, the time it takes for heat to diffuse through the Al film is given by $\tau = L^2C/\Lambda$, which, for the 100 nm film is about 100 ps. Since the thermal properties of interest in TTR are examined over several nanoseconds, in practice, the first 100 ps can be ignored and therefore the thermal properties of the Al film do not affect any of the thermophysical property sensitivities in this work.

Figure 6a shows the sensitivity of the PSTR technique to the thermal conductivity of the substrate with the various substrate diffusivities listed. The PSTR technique is most sensitive for a thermal diffusivity of 10^{-4} $m^2 \cdot s^{-1}$. However, given a single value for the substrate diffusivity, the peak in the sensitivity moves to higher frequencies

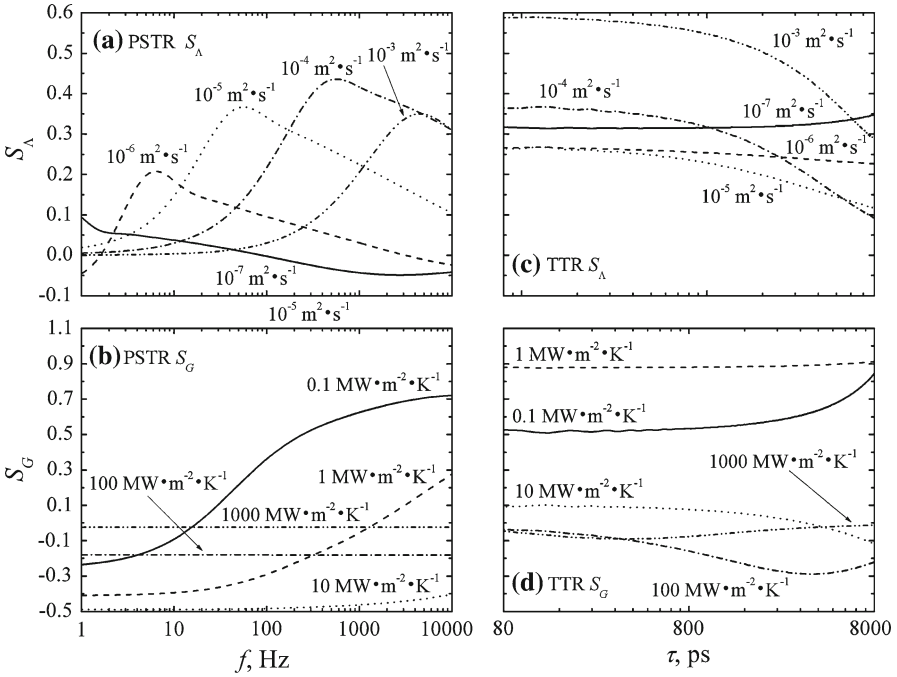

Fig. 6 Sensitivities of the PSTR and TTR responses using Eq. 17 for a 100 nm Al film on substrate systems assuming a range of different values of G and thermal diffusivities of the substrate. The values for G and thermal diffusivities (Λ/C) are listed in the graphs. The thermal diffusivities roughly correspond to a range of thermal conductivities representing water on the low end and diamond on the high end. When calculating S_Λ, it is assumed that $G = 100$ MW $\cdot$ m^{-2} $\cdot$ K^{-1} and $C = 1$ MJ $\cdot$ m^{-3} $\cdot$ K^{-1}; when calculating S_G, Λ is assumed as 100 W $\cdot$ m^{-1} $\cdot$ K^{-1} and C is assumed as 1 MJ $\cdot$ m^{-3} $\cdot$ K^{-1} (i.e., the thermal diffusivity is assumed as 1×10^{-4} m^2 $\cdot$ s^{-1})

as the substrate diffusivity increases. This means that the PSTR technique becomes more sensitive at high frequencies for a high conductivity substrate. Insight into this phenomenon becomes apparent when examining the PSTR sensitivity to G, as seen in Fig. 6b. When G is large, the PSTR technique is relatively insensitive to G in the frequency domain. However, as G decreases, the sensitivity becomes more dynamic and increases in the frequency domain. The reasoning for this and the peaks in the sensitivity of S_Λ in Fig. 6a lie in the relative resistances and thermal penetration depth in the film/substrate system. An increase in f corresponds to a decrease in the thermal penetration depth, D. The PSTR signal will be dominated by the substrate Λ until the penetration depth becomes small so that the majority of the thermal resistance seen by the modulated signal is dominated by the interface and not the depth of the underlying substrate. Therefore, in Fig. 6b, the sensitivity to G increases as the frequency is increased since less of the substrate is probed at higher frequencies and the interface conductance dominates the two resistances. Similarly, in Fig. 6a, an increase in f causes a decrease in the penetration depth which means less of the substrate will be probed, creating a decrease in S_Λ relative to the increase in the signal due to G. The competing trends in sensitivity explain the peak in S_Λ: as the substrate diffusivity is

decreased, the peak sensitivity decreases in frequency since a larger thermal penetration depth is needed to ensure that the thermal resistance of the substrate dominates the thermal resistance associated with the interface; as the frequency decreases even further, the penetration depth becomes so large that the back-side boundary condition (insulated in PSTR) causes a decrease in the ability to accurately determine Λ.

The TTR sensitivities shown in Fig. 6c, d are a bit more intuitive to interpret due to the time domain measurement at a given frequency in TTR. As the thermal penetration depth is always probing the same depth into the substrate, the change in sensitivity is related to how the heat is traveling across the two resistors (interface and substrate) in series. The dynamic sensitivity in the time domain to Λ occurs after the finite amount of time it takes the thermal wave to transmit across the interface. As the substrate becomes less conductive compared to the interface, the temporal sensitivity decreases and the effect of Λ on the signal appears as only a vertical shift in the signal. This is similar to S_G, where a more conductive interface shows dynamic sensitivity in the time domain compared to a less conductive interface.

Figure 7 shows the average TTR sensitivity over the time domain of interest (80 ps to 8 000 ps) divided by the average PSTR sensitivity over the frequency domain of interest (1 Hz to 10 000 Hz) to the thermal conductivity of the substrate and thermal boundary conductance as a function of the thermal diffusivity of the substrate and thermal boundary conductance, respectively. This figure effectively recasts all the cases from Fig. 6 by considering the average sensitivity over the domain, and gives a clear representation of which technique is more sensitive to Λ and G for a range of samples. The sensitivity of TTR clearly dominates PSTR for most samples. However, in samples with thermal diffusivities that offer similar thermal resistances as that offered by G, TTR and PSTR are equally sensitive to Λ. TTR is more sensitive to G than PSTR for most of the range, except for moderate values of G, where the thermal resistance

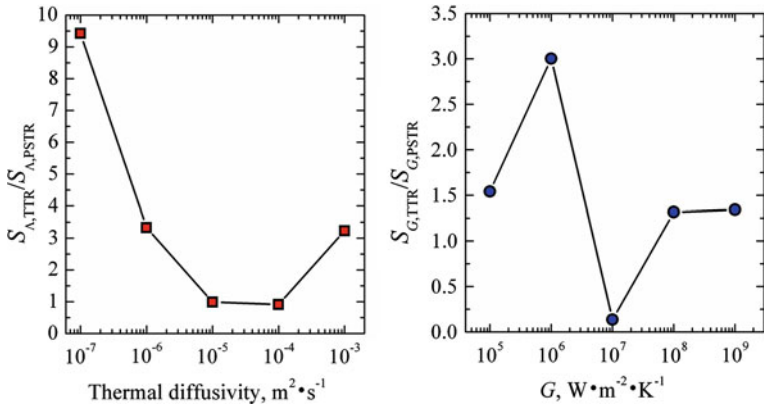

Fig. 7 Average TTR sensitivity over the time domain of interest (80 ps to 8 000 ps) divided by the average PSTR sensitivity over the frequency domain of interest (1 Hz to 10 000 Hz) to the thermal conductivity of the substrate and thermal boundary conductance as a function of thermal diffusivity of the substrate and thermal boundary conductance, respectively. Although the TTR technique is far superior to the PSTR technique in determining G and Λ when the thermal resistance of the substrate of interest is much different than the resistance offered by the interface, the PSTR technique offers more measurement sensitivity to both G and L when the thermal resistances of the interface and substrate are similar

of G is approximately equivalent to the thermal resistance of the underlying substrate. In this case, the TTR model cannot distinguish between the two resistances and PSTR should be used.

As apparent from Figs. 6 and 7, the TTR technique is more sensitive than the PSTR technique over a wider measurement range to both Λ and G. Although the TTR technique is far superior to the PSTR technique in determining G and Λ when the thermal resistance of the substrate of interest is much different than the resistance offered by the interface, the PSTR technique offers more measurement sensitivity to both G and Λ when the thermal resistances of the interface and substrate are similar.

4 Summary

This work compares the sensitivities of the TTR and PSTR techniques for measuring G and Λ in a thin film on substrate material systems. From a solution of the heat equation and implementation of a Feldman algorithm for the temperature change due to a modulated heat source, the temperature changes in TTR (semi-infinite) and PSTR (insulated) measurements are calculated. A parametric study of the sensitivities of each of the thermal models to G and Λ is performed, lending insight into the advantages and disadvantages of each technique. Although the TTR technique is far superior to the PSTR technique in determining G and Λ when the thermal resistance of the nanofilm of interest is much different than the resistance offered by the interface, the PSTR technique offers more measurement sensitivity to both G and L when the thermal resistances of the interface and nanofilm are similar.

Acknowledgment P.E.H. is greatly appreciative for funding from the LDRD program office through the Sandia National Laboratories Harry S. Truman Fellowship. Sandia is a multiprogram laboratory operated by Sandia Corporation, a Lockheed-Martin Company, for the United States Department of Energy's National Nuclear Security Administration under Contract DE-AC04-94AL85000.

References

1. D.G. Cahill, W.K. Ford, K.E. Goodson, G.D. Mahan, A. Majumdar, H.J. Maris, R. Merlin, S.R. Phillpot, J. Appl. Phys. **93**, 793 (2003)
2. D.G. Cahill, K.E. Goodson, A. Majumdar, J. Heat Transf. **124**, 223 (2002)
3. D.G. Cahill, Microscale Thermophys. Eng. **1**, 85 (1997)
4. Y.C. Tai, C.H. Mastrangelo, R.S. Muller, J. Appl. Phys. **63**, 1442 (1988)
5. Y.C. Tai, C.H. Mastrangelo, R.S. Muller, J. Appl. Phys. **66**, 3420 (1989)
6. D.G. Cahill, Rev. Sci. Instrum. **61**, 802 (1990)
7. D.G. Cahill, Rev. Sci. Instrum. **73**, 10 (2002)
8. P.E. Hopkins, L.M. Phinney, J. Heat Transf. **131**, 043201 (2009)
9. L. Shi, D. Li, C. Yu, W. Jang, D. Kim, Z. Yao, P. Kim, A. Majumdar, J. Heat Transf. **125**, 881 (2003)
10. P. Kim, L. Shi, A. Majumdar, P.L. McEuen, Phys. Rev. Lett. **87**, 215502 (2001)
11. Y.K. Koh, S.L. Singer, W. Kim, J.M.O. Zide, H. Lu, D.G Cahill, A. Majumdar, A.C. Gossard, J. Appl. Phys. **105**, 054303 (2009)
12. T. Tong, Y. Zhao, L. Delzeit, A. Kashani, M. Meyyappan, A. Majumdar, IEEE Trans. Compon. Packag. Technol. **30**, 92 (2007)
13. Y. Ohsone, G. Wu, J. Dryden, F. Zok, A. Majumdar, J. Heat Transf. **121**, 954 (1999)
14. B. Li, L. Pottier, J.P. Roger, D. Fournier, Thin Solid Films **352**, 91 (1999)
15. B. Li, J.P. Roger, L. Pottier, D. Fournier, J. Appl. Phys. **86**, 5314 (1999)

16. L. Pottier, Appl. Phys. Lett. **64**, 1618 (1994)
17. C. Chiritescu, D.G. Cahill, N. Nguyen, D. Johnson, A. Bodapati, P. Keblinski, P. Zschack, Science **315**, 351 (2007)
18. R.M. Costescu, D.G. Cahill, F.H. Fabreguette, Z.A. Sechrist, S.M. George, Science **303**, 989 (2004)
19. P.E. Hopkins, P.M. Norris, R.J. Stevens, T. Beechem, S. Graham, J. Heat Transf. **130**, 062402 (2008)
20. P.E. Hopkins, R.N. Salaway, R.J. Stevens, P.M. Norris, Int. J. Thermophys. **28**, 947 (2007)
21. P.E. Hopkins, R.J. Stevens, P.M. Norris, J. Heat Transf. **130**, 022401 (2008)
22. R.J. Stoner, H.J. Maris, Phys. Rev. B **48**, 16373 (1993)
23. A.J. Schmidt, X. Chen, G. Chen, Rev. Sci. Instrum. **79**, 114902 (2008)
24. H.S. Carslaw, J.C. Jaeger, *Conduction of Heat in Solids*, 2nd edn. (Oxford University Press, New York, 1959), p. 109
25. A. Feldman, High Temp. High Press. **31**, 293 (1999)
26. D.G. Cahill, Rev. Sci. Instrum. **75**, 5119 (2004)
27. F. Incropera, D.P. DeWitt, *Fundamentals of Heat and Mass Transfer*, 4th edn. (Wiley, New York, 1996)
28. R.M. Costescu, M.A. Wall, D.G. Cahill, Phys. Rev. B **67**, 054302 (2003)
29. S.-M. Lee, D.G. Cahill, J. Appl. Phys. **81**, 2590 (1997)
30. R.J. Stevens, A.N. Smith, P.M. Norris, J. Heat Transf. **127**, 315 (2005)
31. D.E. Gray, *American Institute of Physics Handbook*, 3rd edn. (McGraw Hill, New York, 1972)